A Zero-Dimensional Lead-Free Hybrid Crystal with Ultra-Low Thermal Conductivity

Md Azimul Haque, Appala Naidu Gandi, Rajeshkumar Mohanraman, Yakui Weng, Bambar Davaasuren, Abdul-Hamid Emwas, Craig Combe, Derya Baran, Alexander Rothenberger, Udo Schwingenschlögl, Husam N Alshareef, Shuai Dong, and Tom Wu**

M. A. Haque, Dr. C. Combe, Prof. D. Baran
KAUST Solar Center (KSC), Physical Science and Engineering Division, King Abdullah University of Science and Technology (KAUST), Thuwal 23955-6900, Saudi Arabia

Dr. A. N. Gandi, Dr. R. Mohanraman, Dr. B. Davaasuren, Prof. A. Rothenberger, Prof. U. Schwingenschlögl, Prof. H. N. Alshareef
Materials Science and Engineering, Physical Science and Engineering Division, King Abdullah University of Science and Technology (KAUST), Thuwal 23955-6900, Saudi Arabia

Dr. Y. Weng, Prof. S. Dong
Department of Physics, Southeast University, Nanjing 211189, China
Email: sdong@seu.edu.cn

Dr. A. H. Emwas
Core Labs, King Abdullah University of Science and Technology (KAUST), Thuwal 23955-6900, Saudi Arabia

Dr. B. Davaasuren
Materials Synthesis and Processing (IEK-1), Institute for Energy and Climate Research, Forschungszentrum Jülich GmbH, 52425 Jülich, Germany

Dr. Y. Weng
School of Science, Nanjing University of Posts and Telecommunications, Nanjing 210023, China

Dr. A. N. Gandi
Department of Metallurgical and Materials Engineering, Indian Institute of Technology Jodhpur, Karwad 342037, India

Prof. T. Wu
School of Materials Science and Engineering, University of New South Wales (UNSW), Sydney, NSW 2052, Australia
Email: tom.wu@unsw.edu.au

Keywords: hybrid material, thermal conductivity, zero-dimensional, tetraiodide

Abstract

Organic-inorganic hybrid materials are of significant interest owing to their diverse applications ranging from photovoltaics, electronics to catalysis. The control over the organic and inorganic components offers flexibility of tuning their chemical and physical properties. In this work, we report that a new organic-inorganic hybrid, $[Mn(C_2H_6OS)_6]I_4$ with linear tetraiodide anions exhibit an ultra-low thermal conductivity of 0.15 ± 0.01 $Wm^{-1}K^{-1}$ at room temperature, which is among the lowest values reported for organic-inorganic hybrid materials. Interestingly, the hybrid compound has a unique zero-dimensional (0D) structure, which extends into three-dimensional (3D) supramolecular frameworks through non-classical hydrogen bonding. Phonon band structure calculations reveal that low group velocities and localization of vibrational energy underlie the observed ultra-low thermal conductivity, which could serve as a general principle to design novel thermal management materials.

Organic-inorganic hybrid materials represent a vast interdisciplinary field of research involving composites, MOFs, biomaterials, to name a few.[1,2] These hybrid materials with a wide spectrum of properties have found important applications in optics, electronics, transportation, health, energy and environmental technologies.[3-5] Particularly, hybrid halide perovskites with the general chemical formula of ABX_3, where A is an organic cation, B is metal cation and X is halide,[6] have recently emerged as promising photovoltaic materials due to their excellent physical properties such as long diffusion length, low trap density, high absorption coefficient, and tunable bandgap.[7-13] The majority of reported hybrid perovskites are Pb or Sn-based, which causes concerns about their toxicity and instability in ambient environment. Some new hybrid materials have been synthesized and tested as light harvesters in solar cells, but their

performance remains modest.[14] The physical properties and potential application of these Pb-free hybrids remain largely unexplored.

In material design, hybrid materials with organic and inorganic moieties could present unique and remarkable new properties absent in the individual constituents.[15] One such property is thermal conductivity, which is of particular interest for applications in thermal insulation, thermoelectrics, microsensors, and thermal data storage.[16-22] Fundamentally, heat conduction and thermal properties of materials are strongly correlated with their atomic structures.[23] In general, very low thermal conductivity is observed in electrically insulating amorphous solids and glasses.[24] The lower limit of thermal conductivity of amorphous solids is well explained by the Einstein limit where the mean free path is assumed to be the same as half of the wavelength of phonons.[25] However, the major bottleneck of employing amorphous low thermal conductivity materials such as silica aerogels is their brittleness, which leads to short lifetimes and higher maintenance costs.[26,27] As a result, there have been efforts to search for low thermal conductivity materials through nanostructure engineering i.e., using thin films, superlattices, nanostructured samples, and disordered crystals.[24,25,28-31] In general, low thermal conductivity in these compounds may arise from material characteristics like strong crystal anharmonicity, complex crystal structure, atomic disorders, large molecular weight, large unit cells or lone pair of electrons, and so on.[32] However, it remains an elusive goal to achieve ultra-low thermal conductivity while maintaining some degree of crystallinity.

Properly designed hybrid organic-inorganic compounds can offer an alternate route to achieve very low thermal conductivity. Hybrid organic-inorganic compounds offer unique advantages such as ease of synthesis, low-temperature processing and large freedom to tailor their properties by manipulating the constituents. These hybrid compounds can primarily be

divided into two categories, hybrid composites and hybrid crystals. Hybrid composites are mostly physical mixtures of two or more materials (organic and inorganic) with random or some degree of ordering of one component in the matrix of the other.[33,34] In the case of hybrid crystals, two different organic and inorganic moieties are integrated into a single crystal structure. Such hybrid crystals can bring unexpected physical and chemical properties although the material design might be more demanding than conventional inorganic and organic materials. It is important to note that the properties of hybrids are not merely the combination of the primary components. Instead, strong synergy effects can occur due to interactions between the organic and inorganic parts that can be further modified by nanoscale confinement.[33] Indeed, ultra-low thermal conductivities of 0.3-0.5 W/(mK) at room temperature were recently reported for organic-inorganic hybrid perovskites. Techniques such as using heater and thermocouple, laser flash method, time-domain thermoreflectance, and scanning near-field thermal microscopy arrived at very similar results and confirmed the ultra-low thermal conductivity of hybrid perovskites.[35-39]

In this contribution, we report on the ultra-low thermal conductivity discovered in a new 0D organic-inorganic hybrid compound[40], hexakis(dimethyl sulfoxide-*k*O)-manganese(II) tetraiodide, $[Mn(C_2H_6OS)_6]I_4$. This hybrid material consists of discrete $[Mn(DMSO)_6]^{2+}$ (DMSO is dimethyl sulfoxide, C_2H_6OS) units connected through non-classical hydrogen bonds to linear I_4^{2-} tetraiodide anions. An ultra-low thermal conductivity of 0.15 $Wm^{-1}K^{-1}$ was obtained at room temperature, which is one of the lowest values reported for hybrid materials. First-principles calculations based on density functional theory elucidate the electronic band structure and predict a bandgap of 1.6 eV. Phonon band structure calculations reveal low group velocities as origin of the low-lattice thermal conductivity.

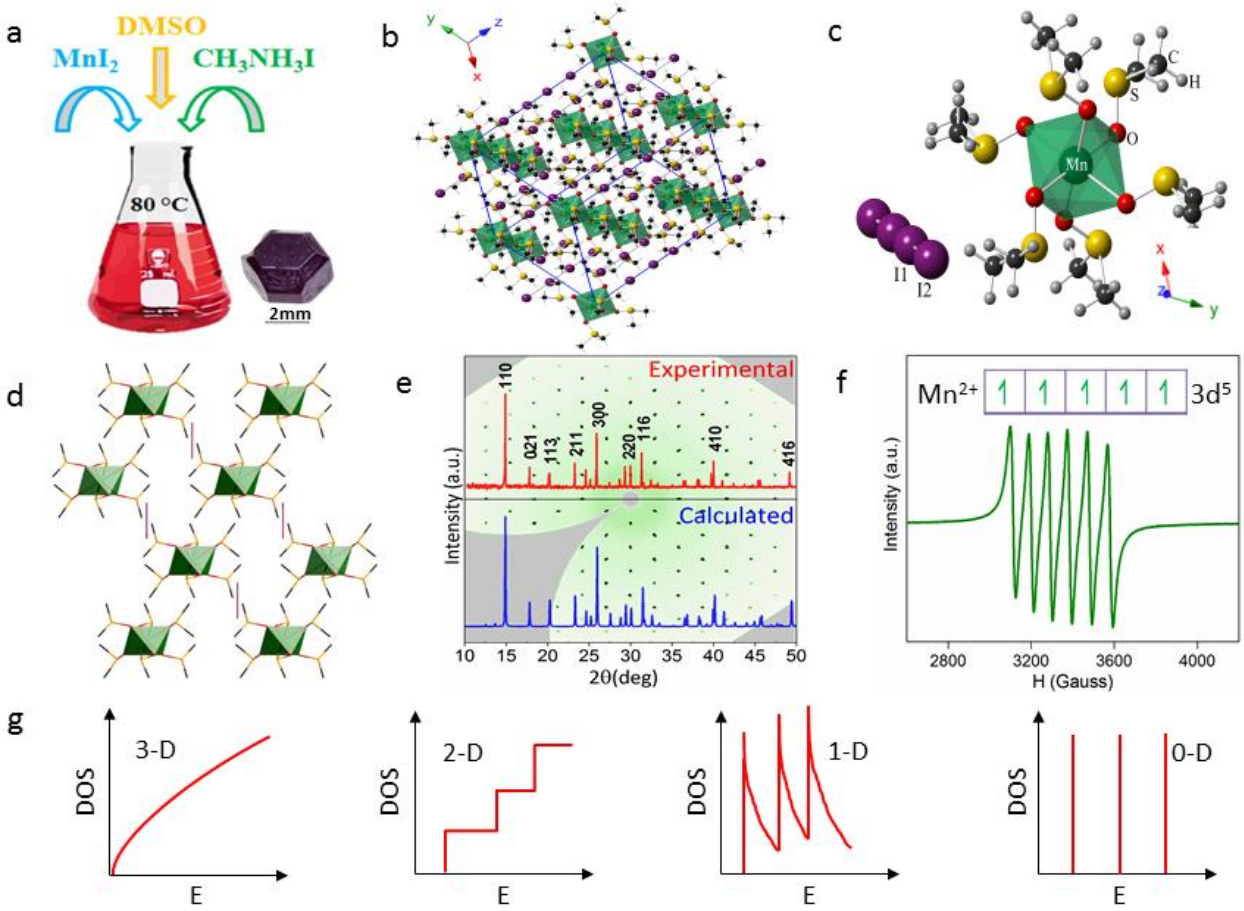

Figure 1. a) Schematic of the MDI single crystal synthesis and a photo of the MDI single crystal. **b)** MDI unit cell. **c)** Ball-and-stick model of the MDI molecules. **d)** Illustration of isolated octahedra in MDI. **e)** Comparison of the observed powder X-ray diffraction pattern of MDI with the calculated diffraction pattern. Further details can be obtained from the Cambridge Crystallographic database quoting the CCDC number 1515632. The reconstructed reciprocal space image of the *hk*0 layer obtained from the single-crystal X-ray diffraction data of MDI is shown in the background. **f)** EPR spectrum confirming the +2 oxidation state of Mn in MDI. **g)** Schematic illustration of the density of states for 3D, 2D, 1D, and 0D materials.

The synthesis of $[Mn(DMSO)_6]I_4$ single crystals is rather simple. A supersaturated solution of methylammonium iodide (MAI) and manganese iodide (MnI_2) in DMSO was mixed and heated in the temperature range of 80-100 °C (**Figure 1**a), with the crystal growth process taking 1-2 days. Interestingly, two different types of single crystals can be obtained depending on the reaction temperature (**Figure S**1). Transparent crystals were grown at 100 °C, while dark colored ones were obtained at 80 °C. Single crystal structure analysis revealed that the

transparent single crystals are $[Mn(DMSO)_6]I_2$ with monoclinic symmetry, which is similar to the compound recently reported by Glatz et al.[41] Because the transparent $[Mn(DMSO)_6]I_2$ single crystals are not stable in ambient condition and they melt into a gel-like state within minutes, we focused our investigation on the dark crystals. $[Mn(DMSO)_6]I_2$ single crystals can be converted into $[Mn(DMSO)_6]I_4$ by dissolving $[Mn(DMSO)_6]I_2$ in ethanol and adding iodine (**Figure S**2). Furthermore, the synthesis process of $[Mn(DMSO)_6]I_4$ can be easily scaled up (**Figure S**3) by employing anti-solvent crystallization technique widely used for the synthesis of hybrid perovskite crystals.[42] We also tried other combinations of organic and inorganic components to explore the possibility of synthesizing new hybrids but did not obtain any stable hybrid compound other than $[Mn(DMSO)_6]I_4$ (**Table S**1). In the following, we denote $[Mn(DMSO)_6]I_4$ as MDI for the simplicity of discussion.

The dark MDI single crystals exhibit excellent stability in ambient environment (**Figure S**4). This compound belongs to the trigonal crystal system (**Table S**2), and in fact it is the first compound with a $[Mn(DMSO)_6]^{2+}$ cation and linear tetraiodide anions.[40] In spite of its fascinating crystal structure, in this work we focus on exploring the thermal properties of MDI single crystals as the compositional fluctuation with the crystal could act to effectively scatter phonons, leading to lower thermal conductivity. The synthesis of MDI is a facile and flexible process. As shown in the reaction schemes below, when stoichiometric amounts of CH_3NH_3I and MnI_2 were mixed, MDI crystals were obtained as the sole solid product (Reaction 1). Further, we discovered that MDI crystals could also be synthesized without the addition of CH_3NH_3I (Reaction 2). In this case, MDI crystals were obtained together with some Mn-containing amorphous solid byproducts (**Figure S**5).

Reaction 1: $MnI_2 + 2CH_3NH_3I + 6(C_2H_6OS) \longrightarrow [Mn(C_2H_6OS)_6]I_4 + C_2H_6 + 2NH_3$

Reaction 2: $2MnI_2 + 6(C_2H_6OS) \longrightarrow [Mn(C_2H_6OS)_6]I_4 + Mn$

In the molecular structure of MDI, the four iodine (I) atoms are arranged in a linear fashion and form non-classical hydrogen bonding with H atoms of the DMSO molecules (**Figure 1**b,c). Interestingly, the bond length between the two central I atoms is shorter than the distance between the central and terminal I atoms. In other words, the central I_2 molecule is weakly bonded to the two terminal I^- anions, forming a linear centrosymmetric polyiodide, which represents a rare example of tetraiodide.[43] Typically, the terminal iodines of the tetraiodides are the only ones forming hydrogen bonds with the methyl group,[44] and the presence of weakly bonded iodines may cause the issues of anion migration and instability in such polyiodides. However, in the case of MDI, all the iodines form hydrogen bonds (**Figure S**6), enhancing the overall structrural stability of the compound. From the crystal structure of MDI, it is clear that the $Mn(DMSO)^{2+}$ octahedra are isolated from each other (**Figure 1**d), suggesting the 0D nature of MDI. These 0D structures then extend to form the 3D supramolecular framework through hydrogen bonding.

The calculated XRD pattern of MDI matches well with the experimental data (**Figure 1**e). The reconstructed reciprocal space image from single crystal XRD measurements in **Figure** 1e confirms the phase purity and high quality of the MDI crystals. We further carried out electron paramagnetic resonance (EPR) measurements to verify the oxidation state of Mn in MDI crystals. Six sharp hyperfine features were observed in the EPR spectrum (**Figure 1**f), confirming the +2 oxidation state of Mn in MDI as a result of the five unpaired electrons in Mn *3d* orbitals. It is well known that the sulfoxides are capable of bonding to transition metals through both S and O atoms.[45] We carried out IR spectroscopy to investigate and confirm the coordination mode of DMSO in MDI. The S-coordinated DMSO ligands exhibit S−O stretching

frequencies in the range of 1080 to 1154 cm^{-1}, while O-bound DMSO ligands exhibit lower vibrational frequencies, ranging from 862 to 997 cm^{-1}.[45] In MDI crystals, stretching frequencies were observed below 1000 cm^{-1}, confirming the coordination of DMSO with Mn through O (**Figure S**7), which supports crystal structure refinement results. In order to confirm the purity of the MDI crystals and to understand the nature of bonding between the C and H atoms, we further performed nuclear magnetic resonance (NMR) analysis. Both ^{1}H and ^{13}C NMR spectra exhibited a single peak as a result of the site symmetry, confirming the phase purity and the presence of only methyl (CH_3) groups (**Figure S**8).

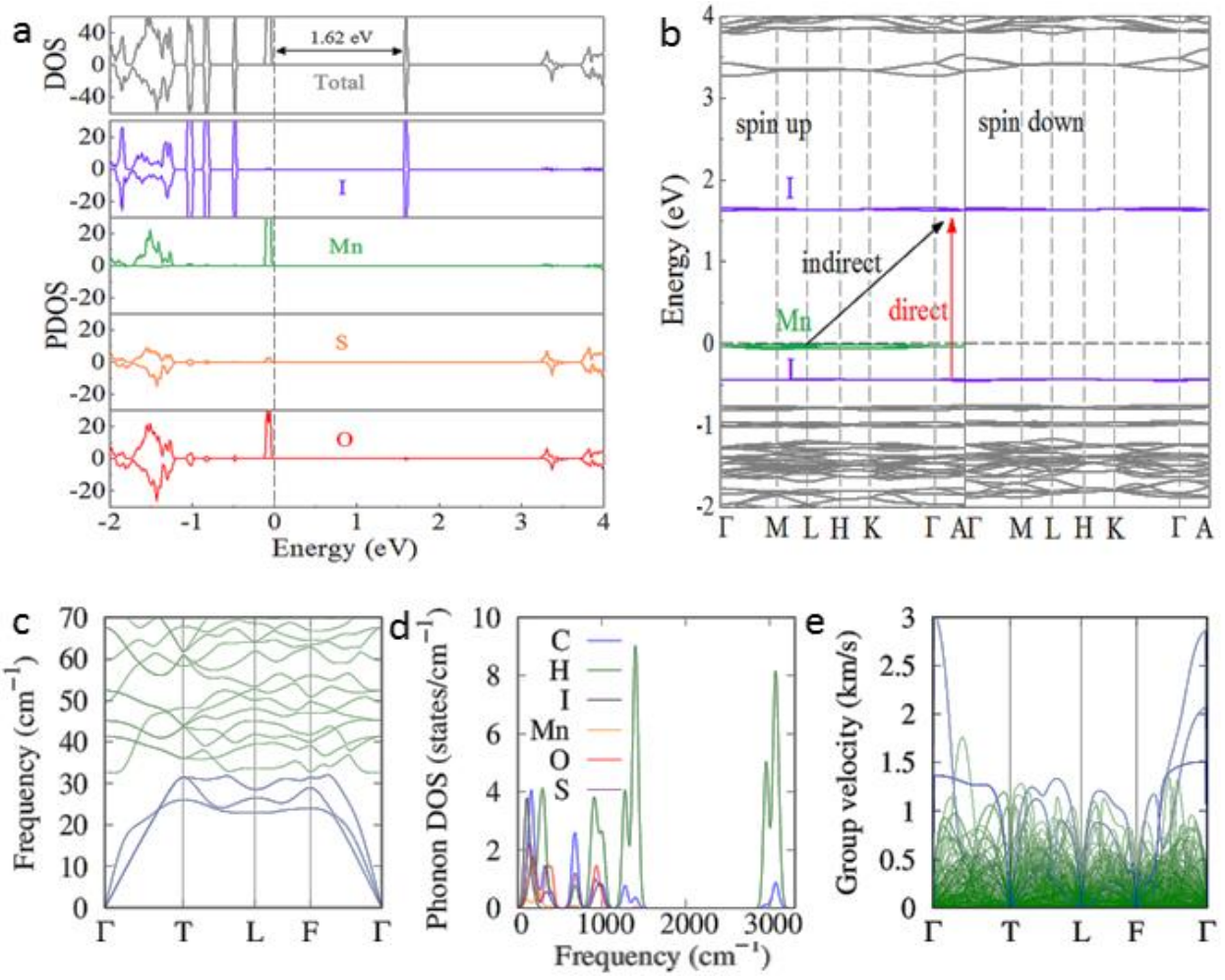

Figure 2. a) DOS and PDOS. **b)** Electronic band structure. **c)** Phonon dispersion. **d)** Phonon PDOS. **e)** Phonon group velocities. In c and e, the blue and green colors represent acoustic and optical phonon branches, respectively.

The dimensionality of materials has a profound influence on their functionalities. Recently, it was found that 1D and 2D materials can have anomalous thermal transport properties,[46,47] but the heat conduction in 0D materials remains largely unknown. Dimensionality reduction can bring striking differences in the electronic density of states (**Figure 1**g), as well as enhanced phonon scattering and lower thermal conductivity in 0D hybrid materials.

First-principles calculations were carried out to elucidate the electronic band structure of MDI. **Figure 2**a shows the total density of states (DOS) and the partial density of states (PDOS) for the individual elements. The sharp peaks, particularly at the conduction and valence band edges, resemble those of quantum dots, and thus can be attributed to the confinement effect. As seen from **Figure 2**b, the band gap is indirect with a value of 1.62 eV, separating the occupied Mn and unoccupied I states (black arrow). There is a gap of 2.06 eV between the occupied and unoccupied I states (red arrow). Due to strong localization of the Mn 3*d* and I 5*p* states, the effective masses of the electrons and holes are expected to be high. We note that the local magnetic moment of the Mn ions is 4.60 μ_B, which is a result of the high-spin state of half-filled t_{2g} and e_g orbitals.

To substantiate the hypothesis of anomalous thermal behaviour, we study the phonon dispersion. As shown in **Figure 2**c, the optical phonon branches are comparatively flat and only the acoustic phonons exhibit some dispersion. The phonon density of states in **Figure 2**d shows a low-frequency region (0-500 cm^{-1}), intermediate frequency region (550-1550 cm^{-1}), and high frequency region (2800-3250 cm^{-1}). All the atoms are involved in the low-frequency phonon modes. In the intermediate-frequency region, the atomic motion involves only atoms in DMSO, i.e., C, H, S, and O. Reflecting the strong C-H bonds, the high-frequency phonon modes involve only the C and H atoms. The largest phonon group velocities are observed for the three acoustic

branches (**Figure 2e**). It is important to note that the average phonon group velocity (both acoustic and optical branches) is 0.17 km/s. For typical semiconductors, such as Si and GaN, the average group velocity is in the range of 4-5 km/s.[48,49] In addition, the optical branches strongly overlap with each other. Recently, very low-phonon lifetimes were reported for hybrid perovskites as a result of overlapped phonon branches.[50] In total, the phonon results point to a very low thermal conductivity in MDI.

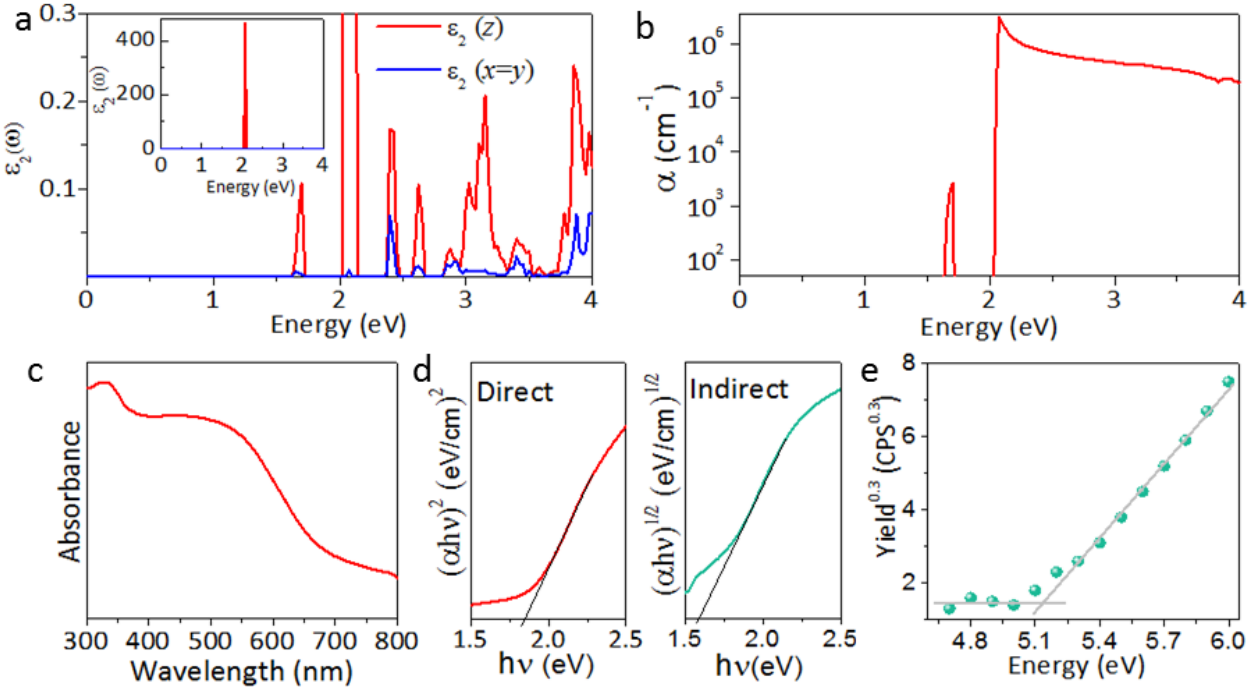

Figure 3. a) Calculated imaginary part of dielectric function. Inset: the view with larger scale of *y*-axis. **b)** Simulated optical absorption coefficient α_z. **c)** Absorption spectra for the MDI single crystals. **d)** Tauc plots showing the direct and indirect nature of MDI bandgap. **e)** PESA measurement showing VBM at −5.11 eV for MDI.

To further characterize the optical properties, the dielectric tensor and optical absorption were calculated. The imaginary component of dielectric constant along the *z*-axis $\mathcal{E}_2(z)$ is much larger than those along the *x*/*y* direction, implying a strong anisotropy of optical absorption in MDI (**Figure 3**a). Interestingly, the MDI single crystal changed its color under polarized light depending on the angle between the incident beam and the crystallographic axis (**Figure S**9).

This unambiguously proves the structural anisotropy of the MDI crystal. In addition, angle-dependent EPR measurement indicates that the MDI crystals possess magnetic anisotropy as well (**Figure S**10). The calculated optical absorption coefficient (α_z, with the electric component of light parallel to the *z*-axis) exhibits a remarkably sharp onset at photon energy of 2.0 eV (corresponds to the direct energy gap between I's bands) and then maintains at a high magnitude of ~10^6 cm^{-1} (**Figure 3**b). Furthermore, there is an optical absorption peak at 1.6 eV, but it is much weaker (~10^3 cm^{-1}) and can be attributed to the indirect energy transition between Mn and I orbitals. Overall, the optical absorption is mostly contributed by I orbitals. The experimental absorption spectrum for the hybrid crystal is shown in **Figure 3**c. The Tauc plots reveal both direct and indirect nature of the bandgap (**Figure 3**d). The optical bandgap of MDI has a lowest-energy direct transition of 1.84 eV and a lowest-energy indirect transition of 1.59 eV. These two values of energy gaps obtained from absorption spectra are very close to the calculated gaps. From photoelectron spectroscopy in air (PESA) measurement, the valence band maxima (VBM) of MDI was estimated to be −5.11 eV (**Figure 3**e).

Thermogravimetric analysis (TGA) and differential scanning calorimetry (DSC) curves measured on the MDI single crystal are shown in **Figure 4**a. The TGA results reveal that the material is thermally stable up to ~200 °C followed by a huge weight loss of 80 % corresponding to the decomposition of MDI. Three well-defined endothermic effects were observed on the DSC, which are associated with melting (124 °C onset point) and decomposition (the latter two) of MDI. To clarify the melting behaviour of the MDI, another TGA/DSC measurement was carried out using fresh MDI single crystals, this time only up to 200 °C. As shown in **Figure 4**b, the heating and cooling curve of the TGA and DSC measurements show characteristic features of the congruent melting behaviour. The powder XRD before and after the DSC did not show any

changes (**Figure S**11), which unambiguously proofs the congruent melting of MDI crystals. It is noteworthy to mention that compounds exhibiting congruent melting can be grown into large single crystals using the Czochralski method.[51]

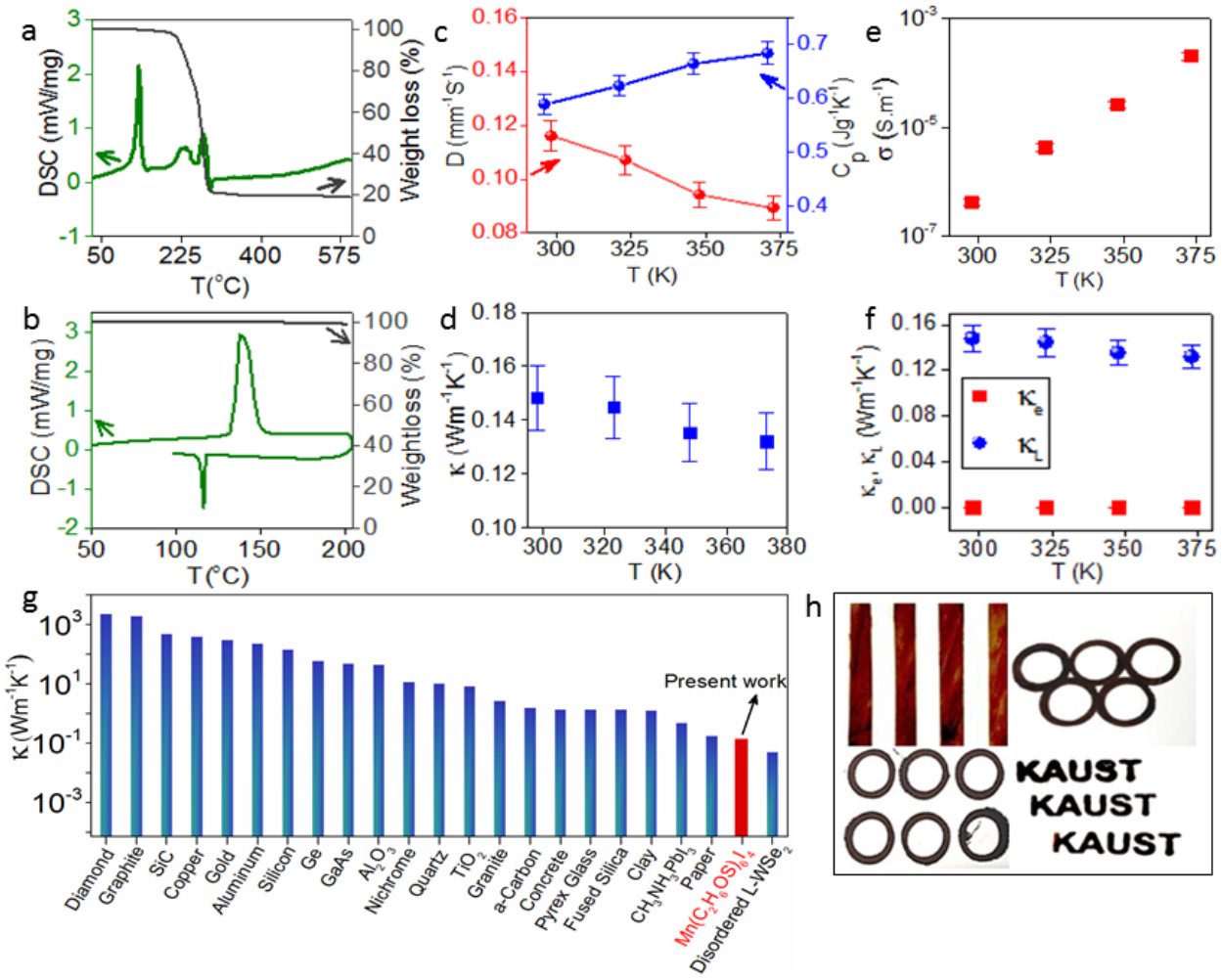

Figure 4. a) DSC and TGA curves. **b)** Heating (melting) and cooling (recrystallization) cycles revealing a congruent melting behaviour. **c)** Thermal diffusivity and specific heat. **d)** Total thermal conductivity. **e)** Electrical conductivity as a function of temperature. **f)** Electronic and lattice contributions to the total thermal conductivity. **g)** Room-temperature thermal conductivity of some typical functional materials in comparison with the hybrid MDI crystal.[24,35,52-54] **h)** Patterns made by stamping the melted MDI at 135 °C.

The facile synthesis of MDI crystals allowed the preparation of large-size pellets for characterizing thermal transport. Scanning electron microscope (SEM) image of the top surface of MDI pellet indicates good packing density (**Figure S**12). Temperature dependence of the

thermal diffusivity, *D*, and the specific heat capacity, C_p, of a MDI pellet are shown in **Figure 4**c. The total thermal conductivity is calculated as a product of the measured C_p, *D*, and mass density (*d*). An ultra-low thermal conductivity of 0.15 ± 0.01 W/mK was derived at room temperature (**Figure 4**d). The total thermal conductivity can be expressed as $\kappa = \kappa_e + \kappa_L$, where κ_e and κ_L are related to charge carriers and lattice phonons, respectively.[55] The electronic contribution, κ_e, can be estimated from the Wiedemann-Franz law, $\kappa_e = L\sigma T$, where $L = 0.7L_0$ (L_0 is the Lorenz factor for free electrons with a value of 2.45×10^{-8} V^2K^{-2}) is used here because the electronic contribution is small[56] and σ is the conductivity of the sample. The electrical conductivity increases with temperature because of the thermal excitation of free carriers (**Figure 4**e). For MDI, the carrier contribution is negligible (κ_e = 3 pW/mK at 298 K). On the other hand, the lattice term (κ_L), which is obtained by subtracting the electrical contribution (κ_e) from κ, contributes more than 99% of the total thermal conductivity (**Figure 4**f). In other words, and the heat is conducted mainly by phonons. This is in line with the resistive nature of MDI; for κ_e to be dominant, a large concentration of free carriers is a prerequisite as in the case of metals.[23] Such negligible κ_e in the same temperature range was previously observed in materials such as $CH_3NH_3PbI_3$ and amorphous Sb_2Te_3.[35,57]

The thermal conductivity achieved in MDI is compared with other typical materials in **Figure 4**g. Furthermore, to check the effect of anisotropy and microstructure, in-plane thermal conductivity was measured by a chip-based 3ω technique using highly oriented MDI films (**Figure S**13). In-plane thermal conductivity of 0.21 ± 0.01 $Wm^{-1}K^{-1}$ was derived at room temperature underscoring the intrinsic nature of constrained heat transport in MDI. Chiritescu and coworkers reported that by making disordered layered crystals, the thermal conductivity of

WSe_2 can be reduced from 1.44 $Wm^{-1}K^{-1}$ to 0.048 $Wm^{-1}K^{-1}$.[24] If disordered 0D materials can be synthesized, even lower thermal conductivity may be achieved.

The present study suggests that the ultra-low thermal conductivity in the 0D MDI may be a general phenomenon and can be extended to other 0D hybrids. One possible reason for the ultra-low lattice thermal conductivity observed in MDI can be partly attributed to its 0D crystal structure with a lot of voids in the unit cell. It is well known that crystals having unit cells with large voids can result in low thermal conductivity.[55] Apart from this, the 0D structure gives rise to a large number of interfaces which increases the phonon scattering, resulting in low thermal conductivity.[58] Recently, several 0D hybrid perovskite crystals were discovered and their optical properties have been reported. Since these 0D perovskite crystals have isolated octahedra similar to MDI, there is a good possibility that these crystals will also exhibit ultra-low thermal conductivity.[59-61] It is noteworthy that taking advantage of the congruent melting nature, MDI can be directly processed into patterns on any given substrates using stamps (**Figure 4**h). This patterning process can be carried out without involving any solvent, which significantly reduces the processing cost. Further improvement of patterning can be achieved using thermal nanoimprint technique similar to the work done on $CH_3NH_3PbI_3$ films.[62] Leveraging the facile melt processing, MDI was incorporated in a simple sandwich structure (ITO/MDI/Pt) to test its photoconduction. Interestingly, the simple diode structure exhibited significant rectification as well as increased conductivity under illumination (**Figure S**14).

To visualize the ultra-low thermal conductivity of MDI, we took infrared images of a MDI pellet on a hot plate heated to 100 °C and compared with reference samples of hybrid perovskite ($CH_3NH_3PbI_3$) and ZnO with identical thickness (**Figure 5**a). Notably, the result show that MDI performs better as a thermal insulator than the perovskite and ZnO. There is a temperature

difference of approximately 25 °C between the hot plate and the MDI pellet surface as observed in the temperature profile (**Figure 5**b). Furthermore, right after the samples were positioned on the hot plate, the temperature of MDI increased much slower than the other two samples (**Figure 5**c), and no saturation was observed even after one hour. The corresponding temperature for MDI, perovskite, and ZnO is 75 °C, 85 °C and 96 °C, respectively, for a hot plate temperature of 100 °C (**Figure 5**d). It is clear that the order of heat transport efficiency is ZnO > Perovskite > MDI, which is consistent with the order of their thermal conductivities.

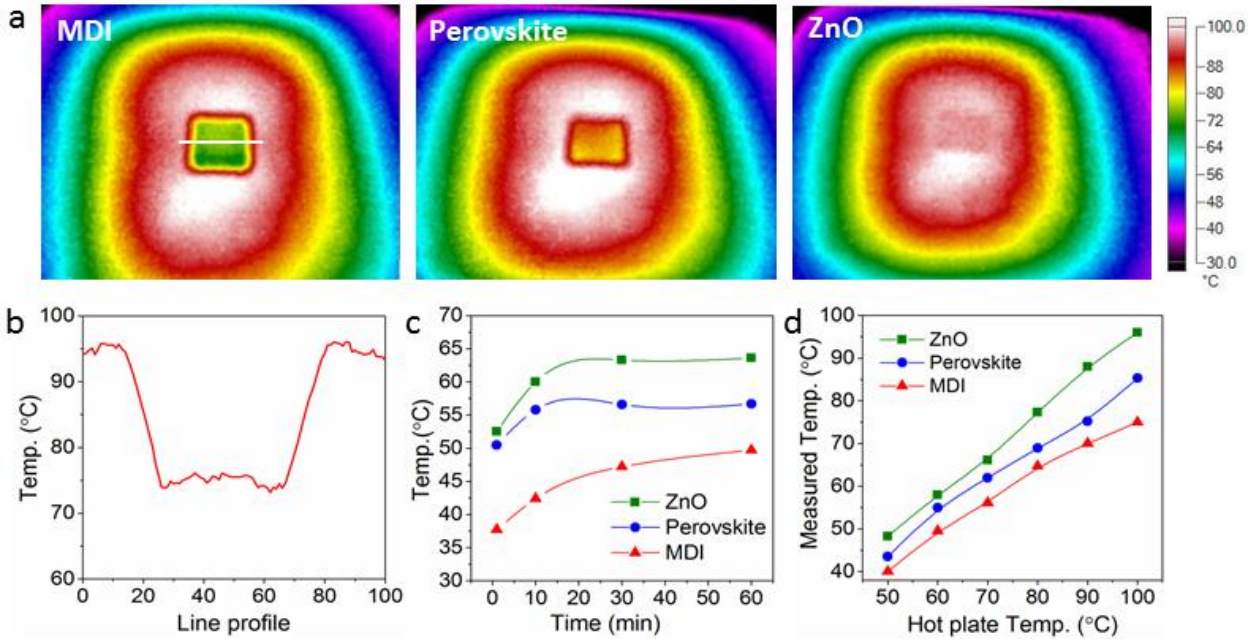

Figure 5. a) Thermal images of MDI, perovskite ($CH_3NH_3PbI_3$), and ZnO at 100 °C. **b)** Line profile passing through the center of the MDI pellet at 100 °C showing the temperature change. **c)** Change in the temperature for MDI, perovskite, and ZnO over time at a constant temperature of 60 °C. **d)** Measured pellet temperature versus hot plate temperature for MDI, perovskite, and ZnO.

In summary, an ultra-low thermal conductivity was discovered in hybrid lead-free $[Mn(C_2H_6OS)_6]I_4$ as a result of its unique 0D crystal structure and low lattice thermal conductivity. The measured thermal conductivity of 0.15 ± 0.01 $Wm^{-1}K^{-1}$ is, one of the lowest among ordered materials, and it could be further reduced by introducing disorders into the

system. Our results suggest that 0D materials have an intrinsic advantage over 3D and other low-dimensional materials to achieve ultra-low thermal conductivity. This material is of particular interest for use as a filler or insulating layers to control the thermal transport in functional materials and composites. Also, if the electrical conductivity can be improved by suitable doping or forming composites with high-mobility materials like carbon nanotubes, while maintaining the ultra-low thermal conductivity, it can lead to efficient thermoelectrics. Furthermore, the present work offers a promising general route for designing 0D materials using organic and inorganic moieties for future materials with exceptional physical properties.

Experimental Section

Materials: Anhydrous MnI_2 (98%) was purchased from Alfa-Aesar and MAI from Dyesol. All other materials were purchased from Sigma-Aldrich and were used as received unless otherwise stated.

Single crystal growth: Single crystals were obtained by cooling a super saturated solution of CH_3NH_3I and MnI_2 in DMSO. MDI crystals can be obtained by heating the solution at 80 °C for 24 hours and then cooling the solution to room temperature and leaving it undisturbed for 1-2 days. $[Mn(DMSO)_6]I_2$ single crystals can be obtained by heating the solution to 100 °C and following the same procedure. We found that the desired MDI single crystals could also be obtained by simple reaction between MnI_2 and DMSO without the addition of MAI, further simplifying the synthesis process. Furthermore, bigger crystals (4-5 mm) can be grown by redissolving small crystals in acetonitrile or acetone at 60 °C and then leaving the solution at room temperature for 3-4 days.

Material characterization: Top view SEM images and EDX spectra were obtained using a field emission scanning electron microscope (FEI-Nova Nano). XRD Powder diffraction patterns were recorded on an STOE STADI MP X-ray diffractometer, equipped with a DECTRIS MYTHEN 1K microstrip solid-state detector. Continuous wave electron paramagnetic resonance (EPR) spectra were recorded using a Bruker EMX PLUS spectrometer equipped with standard resonator for high sensitivity CW-EPR operating at the X-band microwave frequency. Room temperature spectra were recorded at 25 dB microwave attenuation with 5 G modulation amplitude and 100 kHz modulation frequency. Powders of MDI crystals were densified into pellets by cold pressing under 750 MPa for 10 min. The thermal conductivity κ was calculated using the equation $\kappa = D \cdot C_p \cdot d$, where the thermal diffusivity D was obtained using a laser flash apparatus (NETZSCH, LFA 447), specific heat C_p was determined by using a differential scanning calorimeter (NETZSCH, STA 449 F3 Jupiter) and the mass density d was obtained using the Archimedes method. Uncertainties in the D and C_p measurements are ±5% and ±3%, respectively, leading to a 8% uncertainty in the thermal condutivity value. Infrared images of the pellets on hot plate were captured after temperature stabilization using a Fluke TiS40 thermal camera.

Supporting Information
Supporting Information is available from the Wiley Online Library or from the author.

Acknowledgments
The research reported in this publication was supported by funding from King Abdullah University of Science and Technology (KAUST).

References

[1] C. Sanchez, P. Belleville, M. Popall, L. Nicole, *Chem. Soc. Rev.* **2011,** *40*, 696.
[2] A. Rodriguez-Abetxuko, M. C. Morant-Miñana, F. López-Gallego, L. Yate, A. Seifert, M. Knez, A. Beloqui, *Adv. Funct. Mater.* **2018,** *28*, 1803115.
[3] M. Vallet-Regi, M. Colilla, B. Gonzalez, *Chem. Soc. Rev.* **2011,** *40*, 596.
[4] C. Sanchez, B. Julian, P. Belleville, M. Popall, *J. Mater. Chem.* **2005,** *15*, 3559.
[5] P. Yu, K. Hu, H. Chen, L. Zheng, X. Fang, *Adv. Funct. Mater.* **2017,** *27*, 1703166.
[6] M. Gratzel, *Nat. Mater.* **2014,** *13*, 838.
[7] A. Kojima, K. Teshima, Y. Shirai, T. Miyasaka, *J. Am. Chem. Soc.* **2009,** *131*, 6050.
[8] T. M. Brenner, D. A. Egger, L. Kronik, G. Hodes, D. Cahen, *Nat. Rev. Mater.* **2016,** *1*, 15007.
[9] S. D. Stranks, H. J. Snaith, *Nat. Nanotechnol.* **2015,** *10*, 391.
[10] M. I. Saidaminov, M. A. Haque, M. Savoie, A. L. Abdelhady, N. Cho, I. Dursun, U. Buttner, E. Alarousu, T. Wu, O. M. Bakr, *Adv. Mater.* **2016,** *28*, 8144.
[11] J. Cao, B. Wu, R. Chen, Y. Wu, Y. Hui, B. W. Mao, N. Zheng, *Adv. Mater.* **2018,** *30*, 1705596.
[12] Q. Ou, Y. Zhang, Z. Wang, J. A. Yuwono, R. Wang, Z. Dai, W. Li, C. Zheng, Z. Q. Xu, X. Qi, S. Duhm, N. V. Medhekar, H. Zhang, Q. Bao, *Adv. Mater.* **2018,** *30*, 1705792.
[13] S.-T. Ha, C. Shen, J. Zhang, Q. Xiong, *Nat. Photonics* **2015,** *10*, 115.
[14] M. Lyu, J.-H. Yun, P. Chen, M. Hao, L. Wang, *Adv. Energy Mater.* **2017**, 1602512.
[15] X. Huang, M. Roushan, T. J. Emge, W. Bi, S. Thiagarajan, J. H. Cheng, R. Yang, J. Li, *Angew. Chem. Int. Ed. Engl.* **2009,** *48*, 7871.
[16] N. P. Padture, M. Gell, E. H. Jordan, *Science* **2002,** *296*, 280.
[17] I. Chowdhury, R. Prasher, K. Lofgreen, G. Chrysler, S. Narasimhan, R. Mahajan, D. Koester, R. Alley, R. Venkatasubramanian, *Nat. Nanotechnol.* **2009,** *4*, 235.
[18] C. Wan, X. Gu, F. Dang, T. Itoh, Y. Wang, H. Sasaki, M. Kondo, K. Koga, K. Yabuki, G. J. Snyder, R. Yang, K. Koumoto, *Nat. Mater.* **2015,** *14*, 622.
[19]P. Roussel, V. Lysenko, B. Remaki, G. Delhomme, A. Dittmar, D. Barbier, *Sens. Actuator A-Phys.* **1999,** *74*, 100.
[20] X. Xu, J. Chen, J. Zhou, B. Li, *Adv. Mater.* **2018,** *30*, 1705544.
[21] W. Lee, H. Li, A. B. Wong, D. Zhang, M. Lai, Y. Yu, Q. Kong, E. Lin, J. J. Urban, J. C. Grossman, P. Yang, *Proc. Natl. Acad. Sci. U. S. A.* **2017,** *114*, 8693.
[22] Y. Zhao, L. Yang, L. Kong, M. H. Nai, D. Liu, J. Wu, Y. Liu, S. Y. Chiam, W. K. Chim, C. T. Lim, B. Li, J. T. L. Thong, K. Hippalgaonkar, *Adv. Funct. Mater.* **2017,** *27*, 1702824.
[23] A. A. Balandin, *Nat. Mater.* **2011,** *10*, 569.
[24] C. Chiritescu, D. G. Cahill, N. Nguyen, D. Johnson, A. Bodapati, P. Keblinski, P. Zschack, *Science* **2007,** *315*, 351.
[25] R. Prasher, *Phys. Rev. B* **2006,** *74*, 165413.
[26] B. A. Slovick, S. Krishnamurthy, *Appl. Phys. Lett.* **2016,** *109*, 141905.
[27] P. Ruckdeschel, A. Philipp, M. Retsch, *Adv. Funct. Mater.* **2017,** *27*, 1702256.
[28] J. Liu, B. Yoon, E. Kuhlmann, M. Tian, J. Zhu, S. M. George, Y. C. Lee, R. Yang, *Nano Lett.* **2013,** *13*, 5594.
[29] S. R. S. Kumar, M. N. Hedhili, D. Cha, T. M. Tritt, H. N. Alshareef, *Chem. Mater.* **2014,** *26*, 2726.
[30] J. Kang, J. W. Roh, W. Shim, J. Ham, J. S. Noh, W. Lee, *Adv. Mater.* **2011,** *23*, 3414.

[31] M. R. Burton, T. Liu, J. McGettrick, S. Mehraban, J. Baker, A. Pockett, T. Watson, O. Fenwick, M. J. Carnie, *Adv. Mater.* **2018**, 1801357.
[32] Y. Xiao, C. Chang, Y. Pei, D. Wu, K. Peng, X. Zhou, S. Gong, J. He, Y. Zhang, Z. Zeng, L.-D. Zhao, *Phys. Rev. B* **2016,** *94*, 125203.
[33] C. Sanchez, B. Julián, P. Belleville, M. Popall, *J. Mater. Chem.* **2005,** *15*, 3559.
[34] X. Long, J. Li, S. Xiao, K. Yan, Z. Wang, H. Chen, S. Yang, *Angew. Chem.* **2014,** *126*, 7714.
[35] A. Pisoni, J. Jacimovic, O. S. Barisic, M. Spina, R. Gaal, L. Forro, E. Horvath, *J. Phys. Chem. Lett.* **2014,** *5*, 2488.
[36] C. Ge, M. Hu, P. Wu, Q. Tan, Z. Chen, Y. Wang, J. Shi, J. Feng, *J. Phys. Chem. C* **2018,** *122*, 15973.
[37] S.-Y. Yue, X. Zhang, G. Qin, J. Yang, M. Hu, *Physical Review B* **2016,** *94*, 115427.
[38] R. Heiderhoff, T. Haeger, N. PourdavoudP, T. Hu, M. Al-Khafaji, A. Mayer, Y. W. Chen, H. C. Scheer, T. Riedl, *J. Phys. Chem. C* **2017,** *121*, 28306.
[39] G. A. Elbaz, W. L. Ong, E. A. Doud, P. Kim, D. W. Paley, X. Roy, J. A. Malen, *Nano Lett.* **2017,** *17*, 5734.
[40] M. A. Haque, B. Davaasuren, A. Rothenberger, T. Wu, *Acta Cryst. E* **2016,** *72*, 1791.
[41] M. Glatz, M. Schroffenegger, M. Weil, K. Kirchner, *Acta Cryst. E* **2016,** *72*, 904.
[42] D. Shi, V. Adinolfi, R. Comin, M. Yuan, E. Alarousu, A. Buin, Y. Chen, S. Hoogland, A. Rothenberger, K. Katsiev, Y. Losovyj, X. Zhang, P. A. Dowben, O. F. Mohammed, E. H. Sargent, O. M. Bakr, *Science* **2015,** *347*, 519.
[43] D. L. Long, H. M. Hu, J. T. Chen, J. S. Huang, *Acta Cryst. C* **1999,** *55*, 339.
[44] L. Garzón-Tovar, A. Duarte-Ruiz, K. Wurst, *Inorg. Chem. Commun.* **2013,** *32*, 64.
[45] T. Diao, P. White, I. Guzei, S. S. Stahl, *Inorg. Chem.* **2012,** *51*, 11898.
[46] S. Ghosh, W. Bao, D. L. Nika, S. Subrina, E. P. Pokatilov, C. N. Lau, A. A. Balandin, *Nat. Mater.* **2010,** *9*, 555.
[47] R. Fazio, F. W. J. Hekking, D. E. Khmelnitskii, *Phys. Rev. Lett.* **1998,** *80*, 5611.
[48] A. Khitun, A. Balandin, K. L. Wang, *Superlattices Microstruct.* **1999,** *26*, 181.
[49] L. Zhu, H. Luo, *Theor. Appl. Mech. Lett.* **2016,** *6*, 277.
[50] M. Wang, S. Lin, *Adv. Funct. Mater.* **2016,** *26*, 5297.
[51] H. Yu, S. Pan, H. Wu, W. Zhao, F. Zhang, H. Li, Z. Yang, *J. Mater. Chem.* **2012,** *22*, 2105.
[52] F. P. Incropera, D. P. DeWitt, *Fundamentals of Heat and Mass Transfer*. Wiley, New York: **2002**.
[53] P. E. Hopkins, B. Kaehr, E. S. Piekos, D. Dunphy, C. J. Brinker, *J. Appl. Phys.* **2012,** *111*, 113532.
[54] J. H. Kim, D. Seong, G. H. Ihm, C. Rhee, *Int. J. Thermophys.* **1998,** *19*, 281.
[55] G. J. Snyder, E. S. Toberer, *Nat. Mater.* **2008,** *7*, 105.
[56] V. Jovovic, J. P. Heremans, *Phys. Rev. B* **2008,** *77*, 245204.
[57] Q. Li, J. Wei, H. Sun, K. Zhang, Z. Huang, L. Zhang, *Sci.Rep.* **2017,** *7*, 13747.
[58] J. P. Heremans, M. S. Dresselhaus, Recent Developments in Low-Dimensional Thermoelectric Materials. In *Thermoelectrics Handbook*, CRC Press: **2005**; pp 39.
[59] C. Ni, G. Hedley, J. Payne, V. Svrcek, C. McDonald, L. K. Jagadamma, P. Edwards, R. Martin, G. Jain, D. Carolan, D. Mariotti, P. Maguire, I. Samuel, J. Irvine, *Nat. Commun.* **2017,** *8*, 170.
[60] J.-C. Hebig, I. Kühn, J. Flohre, T. Kirchartz, *ACS Energy Lett.* **2016,** *1*, 309.

[61] C. Zhou, H. Lin, Y. Tian, Z. Yuan, R. Clark, B. Chen, L. J. van de Burgt, J. C. Wang, Y. Zhou, K. Hanson, Q. J. Meisner, J. Neu, T. Besara, T. Siegrist, E. Lambers, P. Djurovich, B. Ma, *Chem. Sci.* **2018,** *9*, 586.
[62] N. Pourdavoud, S. Wang, A. Mayer, T. Hu, Y. Chen, A. Marianovich, W. Kowalsky, R. Heiderhoff, H. C. Scheer, T. Riedl, *Adv. Mater.* **2017,** *29*, 1605003.

Intriguing physical and chemical properties of a zero-dimensional organic-inorganic hybrid crystal lead to unique thermal transport. Ultra-low thermal conductivity of 0.15 $Wm^{-1}K^{-1}$ is recorded for $[Mn(C_2H_6OS)_6]I_4$ owing to its zero-dimensional structure and localization of vibrational energy.

Keywords: hybrid, thermal conductivity, zero-dimensional, tetraiodide

Md Azimul Haque, Appala Naidu Gandi, Rajeshkumar Mohanraman, Yakui Weng, Bambar Davaasuren, Abdul-Hamid Emwas, Craig Combe, Derya Baran, Alexander Rothenberger, Udo Schwingenschlögl, Husam N Alshareef, Shuai Dong, and Tom Wu**

A Zero-Dimensional Lead-Free Hybrid Crystal with Ultra-Low Thermal Conductivity

ToC figure